PLOS ONE

RESEARCH ARTICLE

Functional and structural similarity of human DNA primase [4Fe4S] cluster domain constructs

Marilyn E. Holt[ORCID][1], Lauren E. Salay[1], Elizabeth O'Brien[2], Jacqueline K. Barton[2], Walter J. Chazin[ORCID][1]*

1 Departments of Biochemistry and Chemistry, and Center for Structural Biology, Vanderbilt University, Nashville, Tennessee, United States of America, 2 Division of Chemistry and Chemical Engineering, California Institute of Technology, Pasadena, California, United States of America

* walter.chazin@vanderbilt.edu

Abstract

The regulatory subunit of human DNA primase has a C-terminal domain (p58C) that contains a [4Fe4S] cluster and binds DNA. Previous electrochemical analysis of a p58C construct revealed that its affinity for DNA is sensitive to the redox state of the [4Fe4S] cluster. Concerns about the validity of this conclusion have been raised, based in part on differences in X-ray crystal structures of the $p58C_{272-464}$ construct used for that study and that of a N-terminally shifted $p58C_{266-456}$ construct and consequently, an assumption that $p58C_{272-464}$ has abnormal physical and functional properties. To address this controversy, a new $p58C_{266-464}$ construct containing all residues was crystallized under the conditions previously used for crystallizing $p58C_{272-464}$, and the solution structures of both constructs were assessed using circular dichroism and NMR spectroscopy. In the new crystal structure, $p58C_{266-464}$ exhibits the same elements of secondary structure near the DNA binding site as observed in the crystal structure of $p58C_{272-464}$. Moreover, in solution, circular dichroism and $^{15}N,^{1}H$-heteronuclear single quantum coherence (HSQC) NMR spectra show there are no significant differences in the distribution of secondary structures or in the tertiary structure or the two constructs. To validate that the two constructs have the same functional properties, binding of a primed DNA template was measured using a fluorescence-based DNA binding assay, and the affinities for this substrate were the same (3.4 ± 0.5 μM and 2.7 ± 0.3 μM, respectively). The electrochemical properties of $p58C_{266-464}$ were also measured and this p58C construct was able to engage in redox switching on DNA with the same efficiency as $p58C_{272-464}$. Together, these results show that although p58C can be stabilized in different conformations in the crystalline state, in solution there is effectively no difference in the structure and functional properties of p58C constructs of different lengths.

Introduction

DNA synthesis at the replication fork begins with the formation of 8–12 nucleotide (nt) RNA primers on the single-stranded DNA template [1, 2]. In eukaryotes, primers are generated by

Competing interests: The authors have declared that no competing interests exist.

the heterotetrameric DNA polymerase α-primase (pol-prim) complex, which possesses two enzymatic activities in two distinct active sites [3–5]. Primase, a DNA-dependent RNA polymerase, generates the initial hybrid RNA-DNA primed substrate, which is then handed off to DNA polymerase α (pol α) to extend the initial primer by approximately twenty DNA nts. The extended primed substrates are in turn handed off to the processive polymerases ε and δ, which synthesize the bulk of nascent DNA on the leading and lagging strands, respectively [6–8].

Human DNA primase is composed of catalytic (p48) and regulatory (p58) subunits. The regulatory subunit has a C-terminal domain (p58C) that is unique to higher eukaryotes and contains a [4Fe4S] cluster [9–11]. This domain regulates the catalytic efficiency of primase, a function attributed to the ability to bind nucleotides, DNA template, and primed substrate [7, 9, 10, 12–18]. We have recently proposed that [4Fe4S] redox control of DNA binding affinity may serve as a mechanism to drive handoff of the RNA primed template from the primase to the pol α subunits of human pol-prim [19]. Skepticism about some of the reported results have been expressed and debated [20–22], much of which was related to differences in crystal structures obtained from p58C constructs with different N-termini [23].

The p58C domain of human primase has been crystallized under two different conditions and these have generated structures that have the same global fold but localized differences in secondary structures [14, 15]. Fig 1 shows a best-fit superposition of the high-resolution X-ray crystal structures of the two p58C$_{272-464}$ and p58C$_{266-456}$ constructs. The two structures are clearly very similar except for residues Leu318-His351, which are positioned near the DNA binding site. In the crystal structure of p58C$_{272-464}$, these residues occupy a β-sheet-like structure that is stabilized by cross-strand interactions with another molecule in the unit cell [15]. In addition, a disulfide cross-link is formed during crystallization between the Cys449 residues of adjacent p58C molecules. In contrast, when p58C$_{266-456}$ was crystallized under a different set of conditions, this β-type interaction is not observed and instead these residues occupy a helical hairpin [14]. It has been proposed that Ile271 is critical for stabilizing this helical motif and therefore the absence of this residue explains why p58C$_{266-456}$ has a different structure [20, 22].

Many of the concerns about our work were attributed to the fact that the structural differences between the two p58C constructs occurred in a region that contains residues interacting
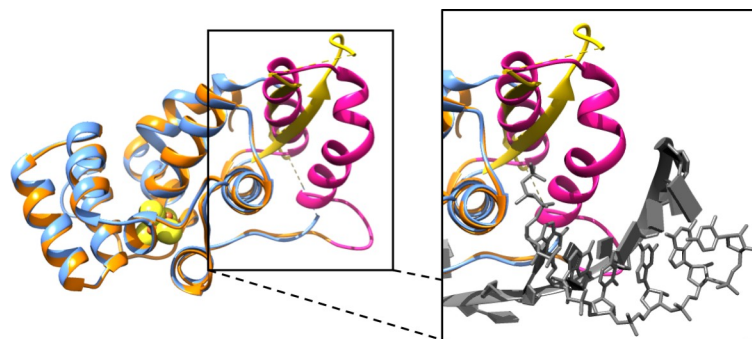
Fig 1. Comparison of the structures of p58C$_{272-464}$ and p58C$_{266-456}$. (A) Best-fit superposition over all backbone atoms of the crystal structures of the p58C$_{272-464}$ (PDB ID: 3L9Q) and p58C$_{266-456}$ (PDB ID: 5F0S) constructs. The substrate in the p58C$_{266-456}$ structure is removed for clarity. Inset: Best-fit superposition over all backbone atoms of the DNA binding region with the primed substrate shown in the p58C$_{266-456}$ structure. p58C$_{266-456}$ is colored orange, p58C$_{272-464}$ blue, and the RNA-primed DNA substrate in grey (RNA in sticks, DNA in slabs). In both panels, Leu318-His351 are colored yellow in the p58C$_{272-464}$ structure and pink in the p58C$_{266-456}$ structure. Connectivity between residues where electron density is missing is indicated by dashed lines.

https://doi.org/10.1371/journal.pone.0209345.g001

with DNA substrates. However, it is well known that differences between crystal structures arise when crystals are formed under different crystallization conditions. In order to resolve any controversy and directly address the concerns raised about our findings, we report here a comprehensive set of studies of a p58C$_{266-464}$ construct. Comparisons of the crystal structure of this construct are made to previously reported crystal structures. In addition, the structure was analyzed in solution by circular dichroism and NMR, along with assays of DNA binding affinities and electrochemical properties. These results show that the structure of Leu318-His351 varies in accord with crystallization conditions, whereas the structure in solution and biochemical properties of different p58C constructs are effectively the same.

Methods

p58C$_{266-464}$ construct generation

The p58C$_{266-464}$ construct was created with a Q5 site-directed mutagenesis kit from New England Biolabs, using the p58C$_{272-464}$ construct plasmid [15] as the template, 5'– GGCAA GATTTCCTTAGATCAGATTGATTTGCTTTCTACC—3' for the forward primer, and 5'–CA CACATTTCCgggcccctggaacagaac—3' for the reverse primer. 10 ng of p58C$_{272-464}$ plasmid was used in the exponential amplification, which was completed as described in the Q5 Site-Directed Mutagenesis Kit manual (New England Biolabs), except that the final extension time was extended to 5 minutes. The KLD reaction was also completed as described in the manual, except that 4 μL of PCR product was used in the reaction and the incubation time was increased to 20 minutes. 10 μL of the KLD reaction product was transformed into XL1-Blue cells. DNA was extracted from individual colonies with a Qiagen QIAprep Spin Miniprep Kit. Appropriate insertion of residues 266–271 was confirmed through plasmid sequencing (GEN-EWIZ, LLC).

Protein expression and purification

p58C constructs were expressed and purified as previously described [19, 23]. In short, plasmid DNA was transformed into BL21 (DE3) cells (Novagen) and cultured in Terrific Broth media at 37˚C to an OD$_{600}$ of 0.6–0.8, when flasks were moved to a 21˚C incubator with shaking. After 30 minutes, ferric citrate and ammonium ferrous citrate were added to a final concentration of 0.1 mg/mL, and isopropyl 1-thio-β-D-galactopyranoside was added to a final concentration of 0.5 mM. Protein was expressed at 21˚C overnight. The same growth protocol was used to generate ^{15}N-labeled p58C, except that cells were cultured in M9 media supplemented with ^{15}N-labled ammonium chloride (Cambridge Isotopes) and expressed overnight at 25˚C. The same purification scheme was used for both unlabeled and ^{15}N-labeled protein [23]. In short, protein was first purified by nickel affinity chromatography (Amersham Biosciences). The 6xHis tag was cleaved with H3C protease and the protein was dialyzed into a low-imidazole buffer [19, 23]. The protein was repassed over the nickel column to remove the H3C protease and uncleaved protein. A heparin column was used as the final purification step to remove residual contaminants [19, 23].

Crystallization and structure determination

The structure of p58C$_{266-464}$ was determined as previously described for p58C$_{272-464}$ [15, 23]. p58C$_{266-464}$ crystals were grown by hanging drop vapor diffusion at 16˚C from a drop composed of equal volumes of 50 mg/ml protein in 20 mM MES (pH 6.5) and 75 mM NaCl and reservoir solution containing 100 mM Tris (pH 8.5), 400 mM Li$_2$SO$_4$ and 18% (v/v) PEG 3350. Prior to data collection, crystals were transferred to a drop containing 100 mM Tris (pH 8.5),

400 mM Li_2SO_4, 18% (v/v) PEG 3350, and 20% (v/v) glycerol for five seconds. The crystals were looped and flash frozen in liquid nitrogen. X-ray data were collected at beamline 21ID-D (Life Sciences Collaborative Access Team) of the Advanced Photon Source at Argonne National Laboratory at 11.5 kEV. All data were processed by HKL2000 [24]. The structure was determined using molecular replacement (PHASER-MR) with PDB entry 3L9Q, residues 274–316 and 360–457, as the search model. Manual model building for the structure was performed using *Coot* model building software, and waters were placed with the *Coot* routine, Find Waters [25]. The final model was obtained by iterative cycles of model building in *Coot* and structure refinement using Phenix.refine in the Phenix suite of programs [26, 27]. Structures were superimposed and RMSD calculated in Chimera with the Matchmaker algorithm [28]. Programs used for structure determination and refinement were accessed through SBGrid [29]. Statistics for data collection and refinement are shown in Table 1.

Table 1. Crystallographic data collection and refinement statistics.

Data collection	
Space Group	C2
Cell Dimensions	
a, b, c (Å)	110.19, 52.56, 88.77
α, β, γ (°)	90, 115.08, 90
Temperature (K)	100
Wavelength (Å)	1.08
Resolution (Å)	50.00–2.01 (2.08–2.01)
Unique Reflections	27193
R_{meas} (%)	0.14 (0.79)
$I/\sigma I$	10.06 (2.12)
Completeness (%)	88.6 (84.4)
Redundancy	3.6 (3.3)
Refinement	
Resolution (Å)	50.00–2.01 (2.08–2.01)
No. reflections	27153
R_{work}/R_{free}	0.18/0.21 (0.23/0.24)
No. molecules/ASU	2
No. atoms	2872
Protein	2689
Ligand/ion	41
Water	52
B-factors	
Mean	39.1
Protein	38.7
Ligand/ion	66.9
R.m.s. deviations	
Bond lengths (Å)	0.003
Bond angles (°)	0.62
Ramachandran	
Favored	308 (99.4%)
Allowed	2 (0.6%)
Disallowed	0 (0%)

Values in parentheses are for the highest-resolution shell.

Circular dichroism (CD) spectroscopy

Samples were buffer exchanged into 20 mM K_2HPO_4 (pH 7.2) and diluted to a concentration of 0.3 mg/mL. The far-UV CD spectrum over the range 190–260 nm was acquired at room temperature using a Jasco J-810 spectrophotometer. Each spectrum is the average of three scans acquired with a scanning rate of 50 nm/min and data pitch of 1 nm. Prior to generating the overlay in Graphpad Prism 7, the $p58C_{266-464}$ spectrum was scaled to the $p58C_{272-464}$ spectrum by averaging the values of the $CD_{208}(p58C_{272-464})/CD_{208}(p58C_{266-464})$ and $CD_{222}(p58C_{272-464})/CD_{222}(p58C_{266-464})$ ratios to generate a scaling factor (~0.86), then multiplying the entire $p58C_{266-464}$ spectrum by this scaling factor.

NMR spectroscopy

Spectra were acquired using a Bruker AV-III 800 MHz spectrometer equipped with a CPTCI single-gradient cryoprobe. ^{15}N-enriched p58C constructs at a concentration of 200 μM were prepared in a buffer containing 20 mM MES (pH 6.5), 50 mM NaCl, 2 mM DTT, and 5% (v/v) D_2O. Two-dimensional ^{15}N-^1H heteronuclear single quantum coherence (HSQC) spectra were acquired at 25°C with 2,048 and 128 points in the ^1H and ^{15}N dimensions, respectively. 64 scans were recorded in the direct (^1H) dimension for each point sampled in the indirect (^{15}N) dimension. Data were processed by Topspin (Bruker) and analyzed with Sparky (University of California).

RNA primer generation

Triphosphorylated RNA primer was transcribed with T7 RNA polymerase [30] and purified on a 25% TBE-polyacrylamide gel supplemented with 8 M urea according to standard methods. Dried RNA pellet was resuspended in RNAse-free H_2O and aliquoted prior to further purification. RNAs used for binding assays were HPLC purified on a Luna 5 μM C18(2) 100 Å 250X4.6 mm column (Phenomenex). Buffer A: 0.1 M ammonium formate; Buffer B: acetonitrile; flow rate: 1.5 mL/min. Purification program: 1–5% Buffer B over three minutes, 5–8% Buffer B over 22 minutes, then 80% Buffer B for five minutes. RNA typically eluted around 11 minutes. HPLC-purified RNA was further validated with mass spectrometry, which confirmed that a product of the expected mass had been generated.

Substrate binding assays

The fluorescence intensity (FI) assay was performed with a Monolith NT.115 series microscale thermophoresis (MST) instrument (NanoTemper) at 25°C. Cy5-labeled 18 nt DNA template was purchased from Sigma-Aldrich. A 1.1:1 ratio of 8 nt RNA and this DNA template was annealed in annealing buffer (20 mM MES (pH 7.0), 75 mM NaCl), resulting in a 25 μM stock of annealed, primed substrate. This stock was diluted to 100 nM with MST buffer (20 mM MES (pH 6.5), 50 mM NaCl, 2 mM DTT, 0.05% Tween). The primed substrate was mixed with p58C and allowed to incubate in the dark at room temperature for 15 min. Samples with a final substrate concentration of 50 nM were then loaded into MO-K003 Monolith NT.115 hydrophobic capillaries (NanoTemper) and fluorescence was measured at 20% LED and 40% MST power. Final K_D values were calculated using the one-site total binding equation in GraphPad Prism 7. Titrations were completed after running an SD test to ensure that the concentration-dependent changes in fluorescence intensity were not due to adsorption to the capillaries or aggregation of the fluorophore [31].

    MST RNA primer: 5'-PPP-GGCUCGGA-3'
    MST DNA template: 5'-Cy5-AAACTCCGAGCCAACATA-3'

Fluorescence anisotropy (FA) was measured with a SpectraMax M5 microplate reader (Molecular Devices). A 6FAM-labeled 22 nt DNA template was purchased from Sigma-Aldrich. A 1.1:1 ratio of 12 nt RNA and this DNA template was annealed in annealing buffer (20 mM MES (pH 7.0), 75 mM NaCl), resulting in a 25 µM stock of annealed, primed substrate. The stock was diluted to 800 nM with DNA binding buffer (20 mM MES (pH 6.5), 50 mM NaCl, 2 mM DTT). This primed substrate was mixed with p58C and allowed to incubate in the dark at room temperature for 15 min. Samples with a final substrate concentration of 50 nM were then loaded into a 384-well plate and polarized fluorescence intensities were measured using excitation and emission wavelengths of 485 nm and 520 nm. The fluorescein control experiments were performed with 25 nM fluorescein (Sigma Aldrich) dissolved in DNA binding buffer containing 0.016% DMSO, which was then mixed with p58C and incubated in the dark at room temperature for 15 min prior to determining fluorescence anisotropy in the same way as for the p58C-DNA titrations. Three replicates were collected for each titration. Final K_D values were calculated using the one-site specific binding equation in GraphPad Prism 7; prior to using this equation, each binding curve was normalized by subtracting the fluorescence anisotropy value of the zero point from each point on the curve. K_D values are reported as the mean ± standard deviation of three measurements for each variant.

FA RNA primer: `5'-PPP-GGACCTCCAGGA-3'`
FA DNA template: `5'-6FAM-AAACTCCTGGAGGTCCAACATA-3'`

Cyclic voltammetry (CV)

Sample preparation for electrochemistry.   Multiplexed chips were fabricated as described previously [19]. p58C construct samples were stored prior to experiments in p58C storage buffer (20 mM Tris (pH 7.2), 75 mM NaCl). All p58C constructs were buffer exchanged into HEPES electrochemistry buffer (20 mM HEPES (pH 7.2), 75 mM NaCl) using Amicon ultra centrifugal filters (0.5 mL, 3 kDa MWCO) (Millipore Sigma). Protein was applied to the filter in volumes of 90–140 µL and centrifuged for 15 minutes at 14000 x g at 4˚C. After centrifugation, 400 µL of HEPES electrochemistry buffer was applied to the filter and centrifuged at 14000 x g for 20 minutes. This was repeated four times to exchange p58C samples into HEPES electrochemistry buffer. After buffer exchange and recovery of sample by centrifugation (2 minutes, 1000 x g), concentrations of [4Fe4S] cluster-containing p58C or mutants were measured by using UV-Visible spectroscopy to monitor the absorbance of the [4Fe4S] cluster at 410 nm (extinction coefficient = 17000 M^{-1} cm^{-1}) [19, 32]. Recovered samples (approx. 100–150 µL in volume) were deoxygenated for 2–3 minutes with argon. Samples were then transferred into the anaerobic chamber (Coy Laboratory products). Prior to deposition onto the gold electrode surface, p58C$_{266-464}$ samples were diluted with previously deoxygenated HEPES electrochemistry buffer to a molar concentration of 40µM [4Fe4S] p58C. Samples were initially deposited onto multiplex chip quadrants in 20 µL volumes and the remaining sample deposited in a well of bulk solution above the chip surface, to a final volume of 200–300 µL.

p58C construct electrochemistry.   All electrochemistry was performed using a CHI620D potentiostat and 16-channel multiplexer (CH Instruments) in an anaerobic glove chamber. Multiplex gold electrodes were part of a three electrode system with an external Ag/AgCl reference electrode (Bioanalytical Systems) and platinum counter electrode. Cyclic voltammetry scans were performed at a scan rate of 100 mV/s over a potential range of +0.412 V to -0.288 V vs. NHE or +0.512 V to -0.188 V vs NHE. Bulk electrolysis on DNA was performed at an applied potential of +0.512 V vs. NHE for all electrochemical oxidation reactions. The oxidizing potential was applied for at least 8.33 minutes for single oxidation reactions on a surface, and 6.67 minutes for the iterative oxidation cycles of p58C variants. The reducing potential

was applied for 8.33 minutes in all electrochemical reduction reactions. All bulk electrolysis and cyclic voltammetry was performed in previously deoxygenated p58C electrochemistry buffer (20 mM HEPES (pH 7.2), 75 mM NaCl). Charge transfer (nC) in the cathodic peak of oxidized samples CV scans was assessed using the area under the current wave of the reduction signal. Charge transfer was measured for oxidized samples using CHI software, assessing the area under the reductive peak in CV after electrochemical oxidation. NTP-dependence of electrochemical signals was measured by pipetting a small volume (1–3 μL) of a 0.1 M ATP stock solution into each quadrant of the multiplexed chip setup. Samples were added by quadrant, as physical barriers in the setup prevent diffusion of NTPs between electrode quadrants. After the volume of ATP stock was deposited onto the electrode quadrant, resulting in a 2.5 mM or 5 mM concentration of ATP in the quadrant, CV scans were measured (100 mV/s scan rate). Charge transfer was assessed using CHI software; charge values were determined by calculation of the area under the reductive and oxidative peak curves. Midpoint potentials of NTP-dependent redox signals were assessed using the peak selection function in CHI software.

Results

p58C can be crystallized in different conformations

To test if the differences between the p58C$_{266-456}$ and p58C$_{272-464}$ structures were a by-product of the differences in sequence, we produced, purified, and crystallized a p58C construct containing residues 266–464 in the conditions used to crystallize p58C$_{272-464}$ [15, 19]. These crystals diffracted to 1.6 Å and the data were phased using molecular replacement with the structure of p58C$_{272-464}$ (3L9Q). To avoid phase bias, residues 315–360 were excluded when defining the search model. With these residues omitted, density for residues in extended conformation that together formed a beta-type interaction were clearly evident in the p58C$_{266-464}$ 2Fo-Fc map (Fig 2).

This region was re-built manually in *Coot*, and the final structure was refined to 2.01 Å resolution. As previously observed for p58C$_{272-464}$ under these conditions, crystallized as a dimer, with a disulfide cross-link between the two Cys449 residues and several stabilizing interactions between symmetry-related molecules (S2 Fig). In p58C$_{266-464}$, residues 330–340 and 353–360 in chain A and 330–345 and 353–359 in chain B are missing due to disorder. Disordered residues in the same regions are observed in the structure of p58C$_{272-464}$. A best-fit superposition of the two structures reveals they are very similar (Fig 3), with a backbone RMSD of only 0.23 Å. This finding shows that the differences in residues Leu318-His351 evident from comparing the previous p58C structures [14, 15, 18] are not intrinsic to the differences in the N-termini of the constructs but rather to differences in the crystallization conditions.
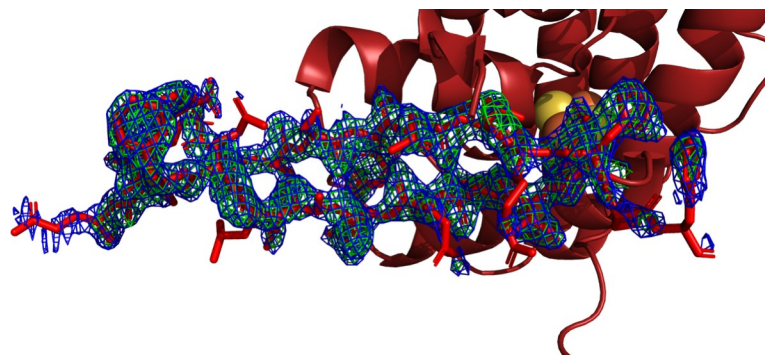
Fig 2. Electron density maps revealing β-sheet-like conformation for residues Leu318-His351. The ribbon diagram of the structure with Leu318-His351 displayed in stick representation is docked into the starting electron density map around the β-sheet-like region. Blue mesh represents the 2F$_o$-F$_c$ map contoured at 1 σ, Green mesh represents the F$_o$-F$_c$ map, contoured at 3 σ. Figure made in Pymol using the isomesh command [33].
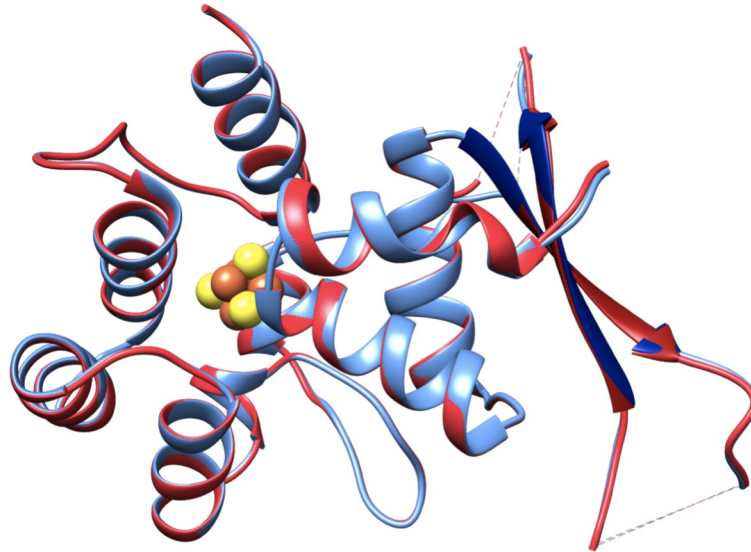
Fig 3. Comparison of the X-ray crystal structures of p58C$_{266-464}$ and p58C$_{272-464}$ obtained from crystals grown under identical conditions. Ribbon diagrams of the best-fit superposition over all backbone atoms of p58C$_{272-464}$ (blue) and p58C$_{266-464}$ (red) crystal structures. Residues Leu318-His351 are colored dark blue in the p58C$_{272-464}$ structure and dark red in the p58C$_{266-464}$ structure. Connectivity between residues where electron density is missing is indicated by dashed lines. The [4Fe4S] clusters are shown as the cluster of yellow and orange spheres.

https://doi.org/10.1371/journal.pone.0209345.g003

CD and NMR show p58C$_{272-464}$ and p58C$_{266-464}$ are structurally similar in solution

Because the differences in the X-ray crystal structures can be attributed to differences in the crystallization conditions, we used CD and NMR spectroscopy to determine if there are significant structural differences between p58C$_{272-464}$ and p58C$_{266-464}$ in solution. The CD spectra of p58C$_{272-464}$ and p58C$_{266-464}$ acquired under identical conditions were very similar (Fig 4), showing that the two constructs contain the same distribution of secondary structure [34]. To further investigate the structures of these constructs, ^{15}N-^{1}H HSQC spectra were collected for ^{15}N-enriched p58C$_{272-464}$ and p58C$_{266-464}$. Fig 5 shows an overlay of HSQC spectra acquired under identical conditions for p58C$_{272-464}$ and p58C$_{266-464}$. These match well with previously published spectra [9, 15], indicating that both constructs are well-folded. There are a number of chemical shift perturbations between the two spectra, consistent with the presence of six additional N-terminal residues. Overall, the distribution of peaks is very similar in the two spectra, indicating that the overall tertiary structure of p58C$_{272-464}$ and p58C$_{266-464}$ are the same. Sequence-specific assignments could provide insight into the nature of the differences in the NMR spectra. However, the presence of the paramagnetic [4Fe4S] cluster causes extreme line broadening due to rapid relaxation of spatially proximate residues, greatly complicating efforts to obtain resonance assignments [35]. Despite the absence of assignments, because the NMR spectra are so similar, and the CD spectra are virtually identical, we can conclude that there are no substantial differences in the structures of p58C$_{272-464}$ and p58C$_{266-464}$ in solution.

The p58C$_{272-464}$ and p58C$_{266-464}$ constructs have the same affinity for a primed template

Having established that the structures of p58C$_{272-464}$ and p58C$_{266-464}$ are essentially the same, it is important to determine if the two constructs are functionally equivalent. Since DNA binding is an essential property for p58C function, we turned to fluorescence assays to compare the
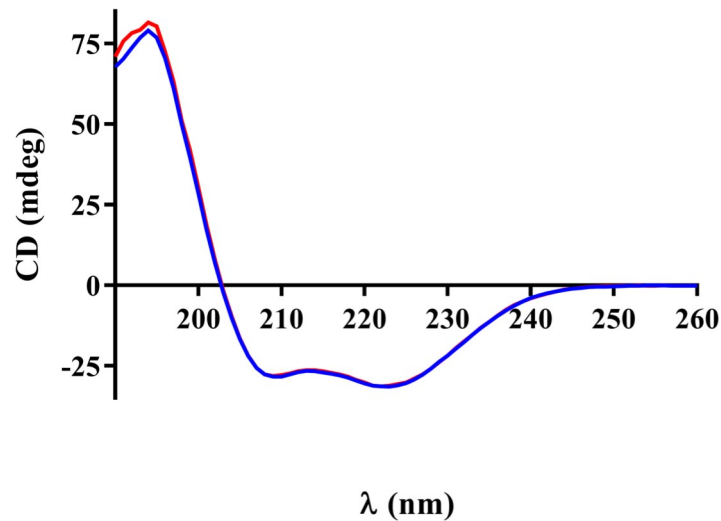
Fig 4. The p58C$_{272-464}$ and p58C$_{266-464}$ constructs have the same distribution of secondary structures in solution.
CD spectra p58C$_{272-464}$ (blue) and p58C$_{266-464}$ (red) were collected at room temperature for a solution containing 0.3 mg/mL of protein in a buffer containing 20 mM K$_2$HPO$_4$ (pH 7.0).

DNA binding properties of the two constructs. We first used a fluorescence intensity (FI)-based assay with an RNA-primed DNA substrate composed of a Cy5-labelled 18 nt DNA template strand annealed with a complementary 5'-triphosphorylated 8 nt RNA primer, corresponding to a high affinity product produced by primase [36]. The affinities of p58C$_{272-464}$ and p58C$_{266-464}$ for this substrate were measured by monitoring initial fluorescence intensity (FI) changes as p58C was titrated into a fluorescently-labelled substrate (Fig 6). Fitting these data to a single site binding equation returned dissociation constants (K$_D$) within statistical error: 2.7 ± 0.3 µM and 3.4 ± 0.5 µM for p58C$_{272-464}$ and p58C$_{266-464}$, respectively.
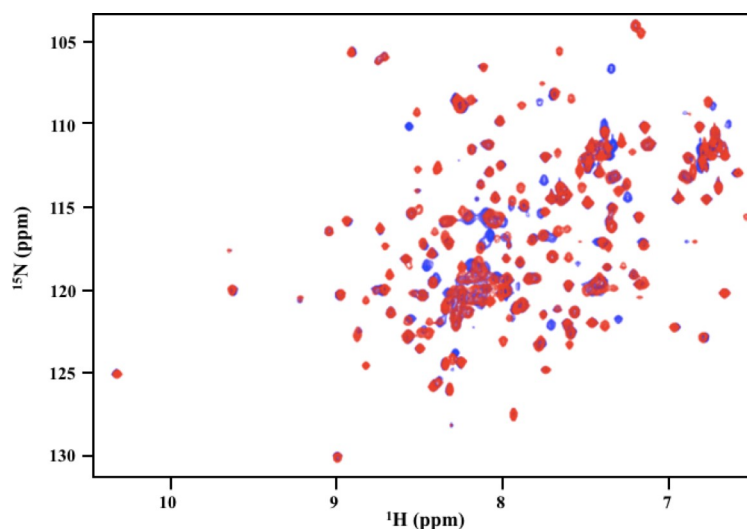
Fig 5. The tertiary structures of p58C$_{272-464}$ and p58C$_{266-464}$ constructs are similar in solution. ^{15}N-^{1}H HSQC NMR spectra of p58C$_{272-464}$ (blue) and p58C$_{266-464}$ (red) were acquired at 25°C on a Bruker AV-III spectrometer operating at 800 MHz. The samples contained 200 µM protein in a buffer containing 20 mM MES (pH 6.5), 50 mM NaCl, 2 mM DTT, and 5% ^{2}H$_2$O.
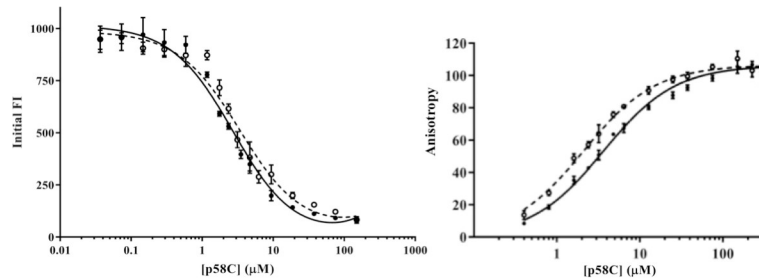
Fig 6. The two p58C constructs bind a RNA-primed substrate with the same affinity. Left: The p58C$_{272-464}$ (filled circle, solid line) and p58C$_{266-464}$ (open circle, dashed line) proteins were titrated into Cy5-labeled substrate in a buffer containing 20 mM MES (pH 6.5), 50 mM NaCl, 2 mM DTT, and 0.05% Tween. FI was measured at 25°C. RNA: 5'-GGCUCGGA-3'; DNA: 5'-Cy5-AAACTCCGAGCCAACATA-3'. Right: The p58C$_{272-464}$ (filled circle, solid line) and p58C$_{266-464}$ (open circle, dashed line) proteins were titrated into 6FAM-labeled substrate in a buffer containing 20 mM MES (pH 6.5), 50 mM NaCl, and 2 mM DTT. Fluorescence anisotropy was measured at 25°C. RNA: 5'-GGACCTCCAGGA-3'; DNA: 5'-6FAM-AAACTCCTGGAGGTCCAACATA-3'. For both panels, error bars represent the standard deviation of three replicates.

Because the fluorescence intensity-based assay is measuring fluorescence quenching, it is conceivable that this assay could be sensing direct interaction with the probe. We turned to a fluorescence anisotropy (FA) assay to measure the binding affinity by an alternate approach and rule out the possibility of direct probe binding. For this assay, an RNA-primed DNA substrate was used composed of a 6FAM-labelled 22 nt DNA template strand annealed with a complementary 5'-triphosphorylated 12 nt RNA primer. We used the longer template to place the probe further away from the RNA-DNA hybrid region and minimize probe quenching. The K$_D$ values of 3.6 ± 0.1 μM and 2.1 ± 0.1 μM obtained by FA for p58C$_{272-464}$ and p58C$_{266-464}$, respectively are very similar to those obtained by the fluorescence intensity assay (Fig 6). To test for direct binding of fluorescein to the p58C constructs, the FA assay was repeated with free fluorescein (see S6 Fig). The absence of binding of fluorescein in these control experiments confirms that the responses in the FI and FA assays are due to interactions between p58C and the DNA substrate. The narrow range (2.1–3.7 μM) and average values (3.2 μM and 2.8 μM, respectively) of K$_D$ for the two constructs measured by the two approaches demonstrate there is no functionally significant difference in the DNA binding properties of these two constructs.

The p58C$_{272-464}$ and p58C$_{266-464}$ constructs have similar electrochemical properties

The [4Fe4S] cluster in p58C$_{272-464}$ was previously shown to function as a redox switch regulating DNA binding and signaling activity [19]. The oxidized, [4Fe4S]$^{3+}$ form of this protein was DNA-bound and redox-active; the reduced [4F-e4S]$^{2+}$ form was loosely associated with DNA and exhibited no DNA-mediated electrochemical signal in a cyclic voltammetry scan. To test whether the same redox switching function was present in p58C$_{266-464}$, we characterized this construct using DNA electrochemistry. Using the multiplexed, DNA-modified Au electrode platform shown in S3 Fig, we assessed the redox behavior of p58C$_{266-464}$ on a 20-nt duplex DNA substrate with a 3-nt, 5'-ssDNA overhang [19]. Electrochemical experiments were performed in anaerobic conditions to prevent nonspecific degradation of the cluster by atmospheric oxygen [37]. Electrochemically unaltered p58C$_{266-464}$, which is predominantly present in the [4Fe4S]$^{2+}$ oxidation state, displays no redox signal on DNA, as observed with p58C$_{272-464}$. However, upon electrochemical oxidation to the [4Fe4S]$^{3+}$ state by bulk electrolysis at an applied potential of 512 mV vs. NHE, CV scans of p58C$_{266-464}$
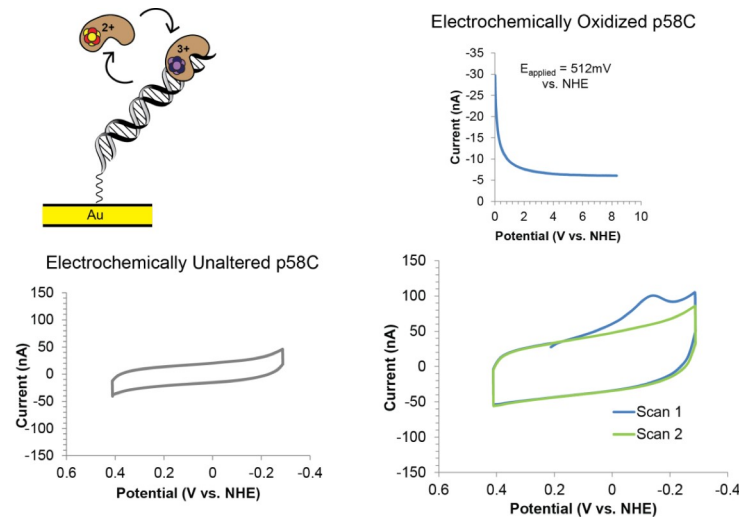
Fig 7. p58C$_{266-464}$ participates in redox switching on DNA. The cartoon (top left) depicts p58C DNA binding and redox switching on an Au electrode. (Bottom left) CV scan of electrochemically unaltered p58C$_{266-464}$. (Right) bulk oxidation (above) of p58C$_{266-464}$ and subsequent CV scans (below). This construct displays similar electrochemical behavior to p58C$_{272-464}$. All electrochemistry was performed in anaerobic conditions with 40 μM [4Fe4S] p58C$_{266-464}$ in 20 mM HEPES (pH 7.2), 75 mM NaCl. CV was performed at 100 mV/s scan rate.

https://doi.org/10.1371/journal.pone.0209345.g007

display a large reductive peak near -140 mV vs. NHE. As observed for p58C$_{272-464}$, this peak disappears after one scan to negative reducing potentials (Fig 7). We next tested if the [4Fe4S] cluster of p58C$_{266-464}$ functions as a redox switch and found that this construct can cycle between the tightly bound, redox-active [4Fe4S]$^{3+}$ state, and the loosely associated [4Fe4S]$^{2+}$ state. The p58C$_{266-464}$ construct also displays a robust, reversible, NTP-dependent signal (S4 Fig) centered at 142 ± 12 mV vs. NHE on a DNA electrode. This is very similar to the signal observed for p58C$_{272-464}$ in the presence of DNA and NTPs, the two necessary substrates for primase activity. Together, these data suggest that the two human p58C constructs, p58C$_{272-464}$ and p58C$_{266-464}$ have the same redox switching ability; the electrochemical function of the [4Fe4S] cofactor is consistent in both proteins.

Discussion

It has been proposed that differences in the structures of residues Leu318-His351 in the crystal structures of p58C$_{266-456}$ and p58C$_{272-464}$ are due to the difference in their N-termini [20, 22]. It has been hypothesized that Ile271 provides critical hydrophobic interactions stabilizing the helical hairpin in the p58C$_{266-456}$ crystal structure and that the absence of this residue leads to misfolding of Leu318-His351 in p58C$_{272-464}$ and formation of β-strands in the p58C$_{272-464}$ crystal structure. As these differences in structure are in the DNA-binding region of p58C, it is plausible to suggest that this may have significant functional repercussions. However, by determining the crystal structure of a new p58C$_{266-464}$ construct with the same extended N-terminal sequence as the p58C$_{266-456}$ construct, we demonstrated that the differences in the previously reported structures were not due to the difference in sequence, but rather to differences in the crystallization conditions.

Analysis of the p58C$_{266-464}$ and p58C$_{272-464}$ crystal structures reveals that substantial crystal lattice packing interactions stabilize this region in both structures. Specifically, Leu318-Gln329 are seen to interact extensively with the same region in the adjacent molecule in the lattice. The backbone atoms between the adjacent molecules in these regions show extensive hydrogen

bonding, stabilizing the beta-like structure. In addition, on both sides of this extended interaction, Phe326 completes a hydrophobic pocket in the adjacent molecule, providing an additional anchor between the two molecules. In the structure of the p58C$_{266-456}$ crystallized under different conditions, a series of stabilizing interactions involve Leu318-His351, but none of these are formed between adjacent molecules in the crystal lattice. A number of crystal contacts in this lattice are found in loop regions and the interfaces of hydrophobic helices. The differences between the crystal contacts in these two models can be attributed to differences in crystallization conditions, most notably the very high concentration of p58C (50 mg/mL) used originally for p58C$_{272-464}$ [23] and now for p58C$_{266-464}$. It is conceivable that at high concentration p58C forms dimers over time promoting the difference in crystal lattice and this in turn may facilitate formation of the inter-molecular Cys449 disulfide.

Crystallization contacts stabilizing alternate conformations of proteins is a well-demonstrated phenomenon [38]. Detailed comparative analysis of crystal structures, structural data obtained in solution, and simulations, have revealed a number of cases in which packing interactions affect backbone and side chain conformations, and even cases of alternate folds [39–41]. The addition of p58C to this group provides additional support for the importance of considering crystallization contacts between adjacent molecules in the crystal lattice when analyzing conformational changes of proteins crystallized with co-factors and ligands.

To further establish the equivalence of the p58C constructs, we turned to structural characterization in solution. Both CD and NMR (Figs 4 and 5) showed that the absence or presence of residues Gly266-Ile271 has no significant impact on structure in solution. DNA binding and cyclic voltammetry assays (Figs 6 and 7) showed that p58C$_{272-464}$ and p58C$_{266-464}$ have effectively the same biochemical properties. The evidence that the DNA binding region of p58C is capable of adapting to different crystallization conditions is consistent with the need for p58C to bind substrates sequence non-specifically, a property often associated with structural plasticity in sequence non-specific DNA binding domains (e.g. [42]). This raises the question: does the structure of p58C change upon DNA binding? One structure of p58C with a DNA substrate bound is available [12]. Comparison of this and the substrate-free structure reveals that only subtle changes in a limited number of side chains is required to bind the substrate [12, 14]. Given the extensive similarities between the p58C structures crystallized in different conditions, there is no reason to think the alternate conformation of residues 318–351 precludes DNA binding. Moreover, at a more fundamental level, it is the structure *in solution* with and without substrate that is required to definitely answer this question. Hence, further solution-state structural characterization of primase in complex with NTPs and primed substrates will be required to establish if there is a functional role for structural plasticity in the template-binding region of p58C.

We note that the approximately 3 µM dissociation constants we observe are similar to those previously reported using fluorescence anisotropy [19], but significantly higher than those reported for p58C$_{266-456}$ binding to a similar substrate measured using an electrophoretic mobility shift assay (EMSA) [36]. Molecular oxygen is known to be generated while running a polyacrylamide gel, which may cause redox-active proteins to become oxidized over the course of an EMSA [32]. As p58C is proposed to bind substrates more tightly when oxidized, we suggest that the EMSA measurements may report the affinity of primarily oxidized p58C, whereas the fluorescence-based measurements report the affinity of the directly purified p58C, which is primarily reduced [9, 19]. Regardless of the differences in the K$_D$ values measured in solution and with EMSAs, our data show the DNA binding affinities of p58C$_{272-464}$ and p58C$_{266-464}$ are effectively the same, indicating that the shorter construct functions normally.

All substrate binding measurements have been performed on p58C in the reduced state. Although a direct assessment of the substrate binding affinity of oxidized p58C is highly

desirable, such experiments are precluded by the instability of the oxidized cluster. Use of chemical oxidants causes degradation of the cluster and precipitation of the protein, as does extended exposure to atmospheric oxygen. Moreover, although the oxidized protein can be generated electrochemically, the lifetime of the oxidized state is not sufficiently long to make a reliable direct measurement of DNA binding affinity by traditional methods. There is substantial interest in developing new approaches that would overcome this challenge.

In summary, we have shown that the absence or presence of residues Gly266-Ile271 does not lead to any significant differences in the structure and biochemical properties of the p58C domain of human DNA primase. Beyond addressing the concerns raised about our initial studies, these data strengthen the support for our proposal that the [4Fe4S] cluster serves as a redox switch that modulates the DNA binding affinity of p58C, setting the stage to further asses the role this switch plays in the priming function of human DNA primase.

Supporting information

S1 Fig. Domain map showing p58C constructs.
(TIF)

S2 Fig. The beta sheet-like region of p58C$_{266-464}$ (red) is stabilized by interactions with the beta sheet-like region of an adjacent symmetry-related molecule (grey).
(TIF)

S3 Fig. Multiplexed, DNA-modified Au electrode platform used for p58C electrochemistry. Sixteen Au electrodes (circles, center) are divided into four quadrants, allowing for electrochemical measurements on different DNA substrates with replicates on a single surface.
(TIF)

S4 Fig. p58$_{256-464}$ Electrochemistry with 2.5 mM ATP. Upon addition of 2.5 mM ATP, a reversible redox signal generally appears in CV scans. The signal in the presence of 2.5 mM ATP was centered at an average midpoint potential measured near 142 ± 12 mV vs. NHE. The signal was observed at physiologically relevant redox potential, with a magnitude on the order of 10^2 nC charge transport. All scans were performed under anaerobic conditions on 40 μM [4Fe4S] p58C in 20 mM HEPES (pH 7.2), 75mM NaCl, at 100mV/s scan rate (CV) or 15 Hz (SQWV).
(TIF)

S5 Fig. Overlays of p58C$_{272-464}$ and p58C$_{266-464}$ ^{15}N-^{1}H HSQC NMR spectra. Overlay of the spectra of p58C$_{272-464}$ (blue) and p58C$_{266-464}$ (red) plotted in the same order (right) and in reverse order (left) relative to Fig 5. These spectra were acquired at 25°C on a Bruker AV-III spectrometer operating at 800 MHz. The samples contained 200 μM protein in a buffer containing 20 mM MES (pH 6.5), 50 mM NaCl, 2 mM DTT, and 5% ^{2}H$_2$O.
(TIF)

S6 Fig. The p58C$_{266-464}$ and p58C$_{272-464}$ constructs do not bind fluorescein. Titrations of p58C$_{272-464}$ (blue circles) and p58C$_{266-464}$ (red squares) into 25 nM fluorescein in a buffer containing 20 mM MES (pH 6.5), 50 mM NaCl, 2 mM DTT, and 0.016% DMSO. Fluorescence anisotropy was measured at 25°C. Before plotting, the data were normalized by subtracting the fluorescence anisotropy value at [p58C] = 0 μM from each titration point. Error bars represent the standard deviation of three independent measurements.
(TIF)

S1 Dataset. Circular dichroism data for p58C$_{266\text{-}464}$ and p58C$_{272\text{-}464}$.
(XLSX)

S2 Dataset. Processed HSQC data for ^{15}N-labeled p58C$_{266\text{-}464}$ and p58C$_{272\text{-}464}$.
(ZIP)

S3 Dataset. Fluorescence intensity data for p58C$_{266\text{-}464}$ and p58C$_{272\text{-}464}$.
(XLSX)

S4 Dataset. Fluorescence anisotropy data for p58C$_{266\text{-}464}$ and p58C$_{272\text{-}464}$ and fluorescein control.
(XLSX)

S5 Dataset. Cyclic voltammetry data for p58C$_{266\text{-}464}$ in the presence of 2.5 mM ATP.
(ZIP)

S6 Dataset. Bulk electrolysis and cyclic voltammetry data for oxidized p58C$_{266\text{-}464}$.
(ZIP)

S7 Dataset. Cyclic voltammetry data for unaltered p58C$_{266\text{-}464}$.
(ZIP)

Acknowledgments

Author Contributions

Conceptualization: Marilyn E. Holt, Walter J. Chazin.

Formal analysis: Marilyn E. Holt, Lauren E. Salay, Elizabeth O'Brien, Walter J. Chazin.

Funding acquisition: Jacqueline K. Barton, Walter J. Chazin.

Investigation: Marilyn E. Holt, Lauren E. Salay, Elizabeth O'Brien.

Methodology: Marilyn E. Holt, Elizabeth O'Brien.

Project administration: Walter J. Chazin.

Supervision: Jacqueline K. Barton, Walter J. Chazin.

Visualization: Marilyn E. Holt, Lauren E. Salay, Elizabeth O'Brien.

Writing – original draft: Marilyn E. Holt.

Writing – review & editing: Marilyn E. Holt, Lauren E. Salay, Elizabeth O'Brien, Jacqueline K. Barton, Walter J. Chazin.

References

1. Stodola JL, Burgers PM. Mechanism of Lagging-Strand DNA Replication in Eukaryotes. Advances in experimental medicine and biology. 2017; 1042:117–33. Epub 2018/01/23. https://doi.org/10.1007/978-981-10-6955-0_6 PMID: 29357056.

2. Burgers PMJ, Kunkel TA. Eukaryotic DNA Replication Fork. Annual review of biochemistry. 2017; 86:417–38. Epub 2017/03/17. https://doi.org/10.1146/annurev-biochem-061516-044709 PMID: 28301743; PubMed Central PMCID: PMCPMC5597965.

3. Sheaff RJ, Kuchta RD. Mechanism of calf thymus DNA primase: slow initiation, rapid polymerization, and intelligent termination. Biochemistry. 1993; 32(12):3027–37. Epub 1993/03/30. PMID: 7681326.

4. Copeland WC, Wang TS. Enzymatic characterization of the individual mammalian primase subunits reveals a biphasic mechanism for initiation of DNA replication. J Biol Chem. 1993; 268(35):26179–89. Epub 1993/12/15. PMID: 8253737.

5. Yao N, O'Donnell M. Bacterial and Eukaryotic Replisome Machines. JSM biochemistry and molecular biology. 2016; 3(1). Epub 2017/01/04. PMID: 28042596; PubMed Central PMCID: PMCPMC5199024.

6. Yeeles JTP, Janska A, Early A, Diffley JFX. How the Eukaryotic Replisome Achieves Rapid and Efficient DNA Replication. Molecular cell. 2017; 65(1):105–16. Epub 2016/12/19. https://doi.org/10.1016/j.molcel.2016.11.017 PMID: 27989442; PubMed Central PMCID: PMCPMC5222725.

7. Baranovskiy AG, Tahirov TH. Elaborated Action of the Human Primosome. Genes (Basel). 2017; 8(2). Epub 2017/02/18. https://doi.org/10.3390/genes8020062 PMID: 28208743; PubMed Central PMCID: PMCPMC5333051.

8. Pellegrini L, Costa A. New Insights into the Mechanism of DNA Duplication by the Eukaryotic Replisome. Trends in biochemical sciences. 2016; 41(10):859–71. Epub 2016/08/25. https://doi.org/10.1016/j.tibs.2016.07.011 PMID: 27555051.

9. Weiner BE, Huang H, Dattilo BM, Nilges MJ, Fanning E, Chazin WJ. An iron-sulfur cluster in the C-terminal domain of the p58 subunit of human DNA primase. J Biol Chem. 2007; 282(46):33444–51. Epub 2007/09/26. https://doi.org/10.1074/jbc.M705826200 PMID: 17893144.

10. Klinge S, Hirst J, Maman JD, Krude T, Pellegrini L. An iron-sulfur domain of the eukaryotic primase is essential for RNA primer synthesis. Nat Struct Mol Biol. 2007; 14(9):875–7. Epub 2007/08/21. https://doi.org/10.1038/nsmb1288 PMID: 17704817; PubMed Central PMCID: PMCPMC2268749.

11. Holzer S, Yan J, Kilkenny ML, Bell SD, Pellegrini L. Primer synthesis by a eukaryotic-like archaeal primase is independent of its Fe-S cluster. Nat Commun. 2017; 8(1):1718. Epub 2017/11/24. https://doi.org/10.1038/s41467-017-01707-w PMID: 29167441; PubMed Central PMCID: PMCPMC5700102.

12. Baranovskiy AG, Babayeva ND, Zhang Y, Gu J, Suwa Y, Pavlov YI, et al. Mechanism of Concerted RNA-DNA Primer Synthesis by the Human Primosome. J Biol Chem. 2016; 291(19):10006–20. Epub 2016/03/16. https://doi.org/10.1074/jbc.M116.717405 PMID: 26975377; PubMed Central PMCID: PMCPMC4858955.

13. Zhang Y, Baranovskiy AG, Tahirov TH, Pavlov YI. The C-terminal domain of the DNA polymerase catalytic subunit regulates the primase and polymerase activities of the human DNA polymerase alpha-primase complex. J Biol Chem. 2014; 289(32):22021–34. Epub 2014/06/26. https://doi.org/10.1074/jbc.M114.570333 PMID: 24962573; PubMed Central PMCID: PMCPMC4139218.

14. Agarkar VB, Babayeva ND, Pavlov YI, Tahirov TH. Crystal structure of the C-terminal domain of human DNA primase large subunit: implications for the mechanism of the primase-polymerase alpha switch. Cell Cycle. 2011; 10(6):926–31. Epub 2011/02/25. https://doi.org/10.4161/cc.10.6.15010 PMID: 21346410; PubMed Central PMCID: PMCPMC3100874.

15. Vaithiyalingam S, Warren EM, Eichman BF, Chazin WJ. Insights into eukaryotic DNA priming from the structure and functional interactions of the 4Fe-4S cluster domain of human DNA primase. Proc Natl Acad Sci U S A. 2010; 107(31):13684–9. Epub 2010/07/21. https://doi.org/10.1073/pnas.1002009107 PMID: 20643958; PubMed Central PMCID: PMCPMC2922289.

16. Zerbe LK, Kuchta RD. The p58 subunit of human DNA primase is important for primer initiation, elongation, and counting. Biochemistry. 2002; 41(15):4891–900. Epub 2002/04/10. PMID: 11939784.

17. Arezi B, Kirk BW, Copeland WC, Kuchta RD. Interactions of DNA with human DNA primase monitored with photoactivatable cross-linking agents: implications for the role of the p58 subunit. Biochemistry. 1999; 38(39):12899–907. PMID: 10504261.

18. Sauguet L, Klinge S, Perera RL, Maman JD, Pellegrini L. Shared active site architecture between the large subunit of eukaryotic primase and DNA photolyase. PLoS One. 2010; 5(4):e10083. Epub 2010/04/21. https://doi.org/10.1371/journal.pone.0010083 PMID: 20404922; PubMed Central PMCID: PMCPMC2852410.

19. O'Brien E, Holt ME, Thompson MK, Salay LE, Ehlinger AC, Chazin WJ, et al. The [4Fe4S] cluster of human DNA primase functions as a redox switch using DNA charge transport. Science. 2017; 355 (6327). https://doi.org/10.1126/science.aag1789 PMID: 28232525; PubMed Central PMCID: PMCPMC5338353.

20. Pellegrini L. Comment on "The [4Fe4S] cluster of human DNA primase functions as a redox switch using DNA charge transport". Science. 2017; 357(6348). Epub 2017/07/22. https://doi.org/10.1126/science.aan2954 PMID: 28729486.

21. O'Brien E, Holt ME, Thompson MK, Salay LE, Ehlinger AC, Chazin WJ, et al. Response to Comments on "The [4Fe4S] cluster of human DNA primase functions as a redox switch using DNA charge

transport". Science. 2017; 357(6348). ARTN eaan2762 https://doi.org/10.1126/science.aan2762 WOS:000405901600002. PMID: 28729485

22. Baranovskiy AG, Babayeva ND, Zhang Y, Blanco L, Pavlov YI, Tahirov TH. Comment on "The [4Fe4S] cluster of human DNA primase functions as a redox switch using DNA charge transport". Science. 2017; 357(6348). Epub 2017/07/22. https://doi.org/10.1126/science.aan2396 PMID: 28729484; PubMed Central PMCID: PMCPMC5741086.

23. Holt ME, Salay LE, Chazin WJ. A Polymerase With Potential: The Fe-S Cluster in Human DNA Primase. Methods Enzymol. 2017; 595:361–90. Epub 2017/09/09. https://doi.org/10.1016/bs.mie.2017.07.002 PMID: 28882207.

24. Otwinowski Z, Minor W. Processing of X-ray diffraction data collected in oscillation mode. Methods Enzymol. 1997; 276:307–26. PMID: 27754618.

25. Emsley P, Lohkamp B, Scott WG, Cowtan K. Features and development of Coot. Acta Crystallogr D Biol Crystallogr. 2010; 66(Pt 4):486–501. https://doi.org/10.1107/S0907444910007493 PMID: 20383002; PubMed Central PMCID: PMCPMC2852313.

26. Adams PD, Afonine PV, Bunkoczi G, Chen VB, Davis IW, Echols N, et al. PHENIX: a comprehensive Python-based system for macromolecular structure solution. Acta Crystallogr D Biol Crystallogr. 2010; 66(Pt 2):213–21. https://doi.org/10.1107/S0907444909052925 PMID: 20124702; PubMed Central PMCID: PMCPMC2815670.

27. Afonine PV, Grosse-Kunstleve RW, Echols N, Headd JJ, Moriarty NW, Mustyakimov M, et al. Towards automated crystallographic structure refinement with phenix.refine. Acta Crystallogr D Biol Crystallogr. 2012; 68(Pt 4):352–67. Epub 2012/04/17. https://doi.org/10.1107/S0907444912001308 PMID: 22505256; PubMed Central PMCID: PMCPMC3322595.

28. Pettersen EF, Goddard TD, Huang CC, Couch GS, Greenblatt DM, Meng EC, et al. UCSF Chimera—a visualization system for exploratory research and analysis. Journal of computational chemistry. 2004; 25(13):1605–12. Epub 2004/07/21. https://doi.org/10.1002/jcc.20084 PMID: 15264254.

29. Morin A, Eisenbraun B, Key J, Sanschagrin PC, Timony MA, Ottaviano M, et al. Collaboration gets the most out of software. Elife. 2013; 2:e01456. Epub 2013/09/17. https://doi.org/10.7554/eLife.01456 PMID: 24040512; PubMed Central PMCID: PMCPMC3771563.

30. Guillerez J, Lopez PJ, Proux F, Launay H, Dreyfus M. A mutation in T7 RNA polymerase that facilitates promoter clearance. Proc Natl Acad Sci U S A. 2005; 102(17):5958–63. Epub 2005/04/16. https://doi.org/10.1073/pnas.0407141102 PMID: 15831591; PubMed Central PMCID: PMCPMC1087904.

31. Linke P, Amaning K, Maschberger M, Vallee F, Steier V, Baaske P, et al. An Automated Microscale Thermophoresis Screening Approach for Fragment-Based Lead Discovery. Journal of Biomolecular Screening. 2016; 21(4):414–21. https://doi.org/10.1177/1087057115618347 PMC4800460. PMID: 26637553

32. Tse ECM, Zwang TJ, Barton JK. The Oxidation State of [4Fe4S] Clusters Modulates the DNA-Binding Affinity of DNA Repair Proteins. Journal of the American Chemical Society. 2017; 139(36):12784–92. Epub 2017/08/18. https://doi.org/10.1021/jacs.7b07230 PMID: 28817778.

33. Schrodinger, LLC. The PyMOL Molecular Graphics System, Version 1.8. 2015.

34. Greenfield NJ. Using circular dichroism spectra to estimate protein secondary structure. Nat Protoc. 2006; 1(6):2876–90. Epub 2007/04/05. https://doi.org/10.1038/nprot.2006.202 PMID: 17406547; PubMed Central PMCID: PMCPMC2728378.

35. Bertini I, Luchinat C, Parigi G, Pierattelli R. NMR Spectroscopy of Paramagnetic Metalloproteins. ChemBioChem. 2005; 6(9):1536–49. https://doi.org/10.1002/cbic.200500124 PMID: 16094696

36. Baranovskiy AG, Zhang Y, Suwa Y, Gu J, Babayeva ND, Pavlov YI, et al. Insight into the Human DNA Primase Interaction with Template-Primer. J Biol Chem. 2016; 291(9):4793–802. Epub 2015/12/30. https://doi.org/10.1074/jbc.M115.704064 PMID: 26710848; PubMed Central PMCID: PMCPMC4813500.

37. Imlay JA. Iron-sulphur clusters and the problem with oxygen. Mol Microbiol. 2006; 59(4):1073–82. https://doi.org/10.1111/j.1365-2958.2006.05028.x WOS:000234800600001. PMID: 16430685

38. Eyal E, Gerzon S, Potapov V, Edelman M, Sobolev V. The limit of accuracy of protein modeling: influence of crystal packing on protein structure. J Mol Biol. 2005; 351(2):431–42. Epub 2005/07/12. https://doi.org/10.1016/j.jmb.2005.05.066 PMID: 16005885.

39. Diener JL. Complex conformations and crystal contacts. Nat Struct Biol. 2003; 10(7):494; author reply -5. Epub 2003/06/26. https://doi.org/10.1038/nsb0703-494a PMID: 12825083.

40. Layten M, Hornak V, Simmerling C. The open structure of a multi-drug-resistant HIV-1 protease is stabilized by crystal packing contacts. Journal of the American Chemical Society. 2006; 128(41):13360–1. Epub 2006/10/13. https://doi.org/10.1021/ja065133k PMID: 17031940; PubMed Central PMCID: PMCPMC2532084.

41. Taylor P, Dornan J, Carrello A, Minchin RF, Ratajczak T, Walkinshaw MD. Two structures of cyclophilin 40: folding and fidelity in the TPR domains. Structure. 2001; 9(5):431–8. Epub 2001/05/30. PMID: 11377203.

42. Arunkumar AI, Stauffer ME, Bochkareva E, Bochkarev A, Chazin WJ. Independent and coordinated functions of replication protein A tandem high affinity single-stranded DNA binding domains. J Biol Chem. 2003; 278(42):41077–82. Epub 2003/07/26. https://doi.org/10.1074/jbc.M305871200 PMID: 12881520.